Research Square

Preprints are preliminary reports that have not undergone peer review.
They should not be considered conclusive, used to inform clinical practice,
or referenced by the media as validated information.

Multi-satellite constraints reduce uncertainty in modeled aerosol forcing

Yusuf Bhatti

y.bhatti@sron.nl

SRON Space Research Organisation Netherlands

Leighton Regayre

University of Leeds

Hailing Jia

SRON Space Research Organisation Netherlands

Duncan Watson-Parris

Scripps Institution of Oceanography

Nick Schutgens

Vrije Universiteit

Athanasios Nenes

Ecole Polytechnique Fédérale de Lausanne (EPFL)

Ulas Im

Aarhus University

Bastiaan van Diedenhoven

Space Research Organisation Netherlands (SRON)

Ardit Arifi

SRON Space Research Organisation Netherlands

Guangliang Fu

SRON Space Research Organisation Netherlands

Xuemei Wang

The Royal Netherlands Meteorological Institute

Carl Svenhag

Aarhus University

Gerd-Jan van Zadelhoff

The Royal Netherlands Meteorological Institute

Otto Hasekamp

SRON Netherlands Institute for Space Research

Article

Keywords:

Posted Date: November 16th, 2026

DOI: https://doi.org/10.21203/rs.3.rs-11566798/v1

License: This work is licensed under a Creative Commons Attribution 4.0 International License.
Read Full License

Additional Declarations: No competing interests reported.

Multi-satellite constraints reduce uncertainty in modeled aerosol forcing

Yusuf Bhatti[1*], Leighton Regayre[2,3,4], Hailing Jia[1], Duncan Watson-Parris[5], Nick Schutgens[6], Athanasios Nenes[7,8], Ulas Im[9], Bastiaan van Diedenhoven[1], Ardit Arifi[1], Guangliang Fu[1], Xuemei Wang[10], Carl Svenhag[9], Gerd-Jan van Zadelhoff[10], Otto Hasekamp[1]

[1]SRON Space Research Organisation Netherlands, Leiden, Netherlands.
[2]Met Office Hadley Centre, Exeter, UK.
[3]Centre for Environmental Modelling and Computation, University of Leeds, Leeds, UK.
[4]School of Earth and Environment, University of Leeds, Leeds, UK.
[5]Scripps Institution of Oceanography and Halıcıoğlu Data Science Institute, University of California San Diego, La Jolla, CA, USA.
[6]Vrije Universiteit Amsterdam, Amsterdam, Netherlands.
[7]Institute of Chemical Engineering Sciences, FORTH/ICE-HT, Patras, Greece.
[8]School of Architecture, Civil and Environmental Engineering (ENAC), Laboratory of Atmospheric Processes and their Impacts (LAPI), Ecole Polytechnique F'ed'erale de Lausanne (EPFL), Lausanne, Switzerland.
[9]Aarhus University, Department of Environmental Science, Roskilde, Denmark.
[10]Royal Netherlands Meteorological Institute (KNMI), Utrecht, Netherlands.

*Corresponding author(s). E-mail(s): y.bhatti@sron.nl ;

Abstract

Aerosol interactions with radiation and clouds remain a dominant source of uncertainty in climate models, limiting confidence in historical climate attribution and future projections. Attempts to reduce the uncertainty in this aerosol Effective Radiative Forcing (ERF) with satellites have relied mainly on cloud observations, leaving the aerosol emissions, properties, and processes that drive it poorly constrained. The recently launched Plankton, Aerosol, Cloud and ocean Ecosystem (PACE) and the Earth Cloud, Aerosol, and Radiation Explorer (EarthCARE) satellites measure aerosol amount, size, absorption, and vertical distribution with high accuracy, together with heritage cloud droplet number retrievals, opening up opportunities to reduce ERF uncertainty. Here, we show that the use of these satellite observations in combination with the ECHAM-HAM aerosol-climate model reduces the parametric ERF uncertainty (90% confidence range) by 34% from 1.35 W m^{-2} to 0.90 W m^{-2}, constraining the forcing from both aerosol-radiation (66%) and aerosol-cloud interactions (31%). We find an observation-consistent ERF of -1.52 [-2 to -1.1] W m^{-2}. This suggests that, from the current IPCC range [-2.0 to -0.6] W m^{-2}, the values <-1.1 W m^{-2} are most likely, indicating stronger aerosol cooling.

Introduction

Clouds and aerosols play a central role in Earth's radiative energy balance and remain a dominant uncertainty in estimates of anthropogenic effective radiative forcing (ERF) [1]. Aerosols affect climate directly by scattering and absorbing radiation (aerosol-radiation interactions; ERF_{ari}), and indirectly (aerosol-cloud interactions; ERF_{aci}) by acting as cloud condensation nuclei, which modify cloud properties and precipitation [2, 3]. Since the start of the industrial period, changes in anthropogenic emissions have driven substantial cooling, offsetting part of the greenhouse-gas warming [1, 2].

Despite major advances in climate models and observations, aerosol effective radiative forcing remains the largest uncertainty in estimates of anthropogenic climate forcing [1, 2, 4, 5]. Some of the inter-model spread [6] may stem from tuning models (with inherent structural errors) using a limited observational dataset, thereby correcting one aspect at the expense of others [7, 8].

Aerosol ERF is not directly observable. Constraining ERF in climate models, therefore, requires measuring aerosol and cloud properties that influence ERF, which can be compared with model diagnostics in a consistent sampling framework [7, 9, 10]. Perturbed parameter ensembles (PPE) provide an effective tool to map observable quantities onto ERF and, therefore, identify which processes control ERF uncertainty [4, 11–15].

Most studies that aimed to constrain model ERF uncertainty using a PPE with observations faced limitations related to structural model errors [7, 8], observational uncertainties and representation errors [16–18], or an insufficient number of parameters being perturbed [10]. Also, for these studies, the theoretical capability of constraining ERF with their observational data set remains unclear. The studies using satellite observations were primarily limited to cloud properties [8, 12, 19, 20]. Here, Regayre et al. [8] obtained a relatively tight constraint, but only after reducing the total number of observations to 13 out of 450. Adding more observations would substantially weaken their constraint to one similar to Johnson et al. [10], pointing to structural model errors and/or observational limitations. With so few observations, there is a risk of overfitting, which may constrain ERF towards the wrong value (e.g., in case of observational biases). Studies that aimed to constrain model ERF using aerosol observations have so far been restricted to ground-based or aircraft aerosol measurements [10, 21, 22], and sometimes with global mean AOD from satellites [9]. A limitation of the use of ground-based or aircraft measurements is the presence of relatively large representation errors [16], as well as structural model errors (e.g., in transport) [8] that hamper modeling of a specific quantity for a specific grid cell but do not affect the broader spatial patterns that matter for ERF.

Here we use satellite observations of aerosol amount, size, absorption, and vertical distribution, in addition to cloud droplet number concentrations (N_d), to constrain a PPE of aerosol climate model simulations from the ECHAM6.3-HAM2.3 model

[23, 24]. The Plankton, Aerosol, Cloud and ocean Ecosystem (PACE; February 2024 [25, 26]) and the Earth Cloud, Aerosol, and Radiation Explorer (EarthCARE; May 2024, [27]) satellites provide the above-mentioned aerosol properties with high accuracy [28–30]. We first perform a synthetic experiment to show that these observations have the theoretical capability to constrain ERF. For real observations, we find a constraint on ERF that is consistent with the different aerosol and cloud properties, producing a robust reduction in ERF uncertainty. We find a strong constraint on natural aerosol and biomass burning emissions, absorption properties, and droplet activation. The combined constraints produce a coherent shift in aerosol forcing and reduce ERF uncertainty by about 34%, where ERF_{ari} uncertainty decreases by 66%, and ERF_{aci} by 31%. The observationally consistent ERF ensemble mean is -1.5 W m^{-2} (5–95%: -1.97 to -1.07 W m^{-2}), which is 0.4 W m^{-2} more negative (cooler) than the control run. Our range lies within the IPCC Sixth Assessment Report (AR6) range of -2.0 to -0.6 W m^{-2}, but has a more negative (cooler) mean than the AR6 best estimate of -1.3 W m^{-2} and excludes the values -1.1 to -0.6 W m^{-2}, suggesting that constraining these model parameters using aerosol satellite observations from PACE and EarthCARE favors a stronger aerosol cooling [1, 31].

Results

Satellite constraint on ERF

We constrain a perturbed parameter ensemble (PPE) of the ECHAM6-HAM climate model (See Materials), in which 28 parameters controlling aerosol emissions, optical properties, chemistry, removal, new particle formation, and cloud droplet activation are perturbed simultaneously across 250 simulations (Supplementary Table 1). We use observations from PACE/SPEXone of fine- and coarse aerosol optical depth (AOD), Aerosol Index (AI - the product of total AOD and Angstrom Exponent), Single Scattering Albedo (SSA), PACE/OCI cloud droplet number concentration (N_d), and

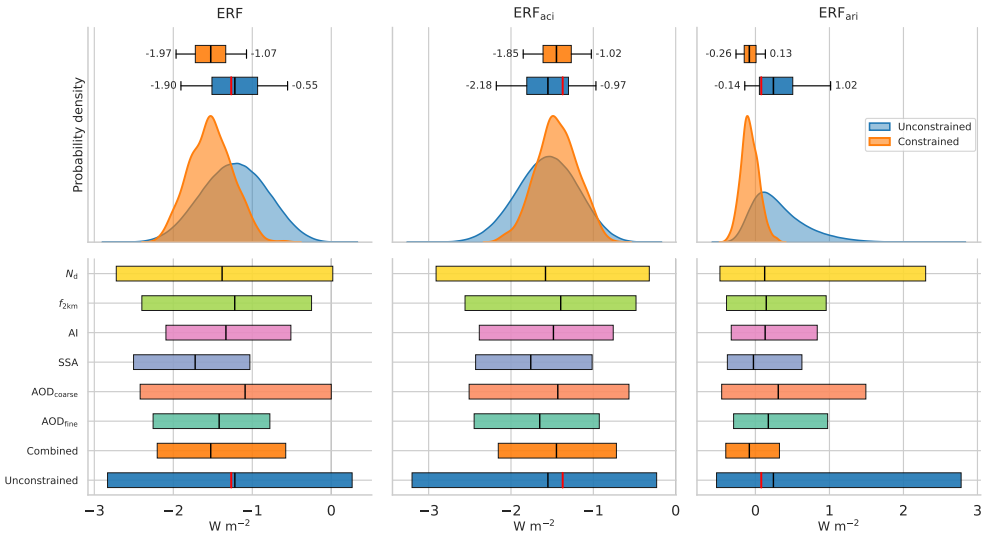


Fig. 1 Global annual-mean probability density functions of aerosol forcing in the emulated PPE (2 million variants) for (left) total aerosol ERF, (middle) ERF$_{aci}$, and (right) ERF$_{ari}$. In each top panel, the unconstrained ensemble (blue) and the joint-constrained ensemble (orange; 1290 variants) are shown as probability densities, with boxplots indicating the interquartile range and median. The black lines represent their average values, and the red vertical line represents the mean control simulation. The whisker values represent the 5th to 95th percentile range. Bottom panels show the minimum-to-maximum range for the constraint directly from each individually applied observational constraint (AOD$_{\mathrm{fine}}$, AOD$_{\mathrm{coarse}}$, SSA, AI, f$_{2\mathrm{km}}$, N$_d$), relative to the unconstrained ensemble.

fraction of aerosol extinction below 2 km in the atmosphere from EarthCARE/ATLID (f$_{2\mathrm{km}}$) (monthly mean values for 18 regions, see Supplementary Fig. 1, with hemispheric contrast as an extra constraint target for N_d). To highlight the added value of PACE and EarthCARE satellite retrievals for constraining ERF, we first perform a synthetic experiment spanning the full prior ERF range (-2.3 to -0.2 W m^{-2}) where 500 model variants served as a known truth to generate synthetic observations. We included realistic errors on the PACE and EarthCARE synthetic aerosol/cloud observations (Methods), and applied our constraint method (see Methods). For the synthetic experiment, the joint constraint has an ERF with negligible bias (0.01 W m^{-2}), a root-mean-square error of 0.17 W m^{-2}, and a 90% credible interval of 0.55 W m^{-2} (Supplementary Fig. 2). This highlights that with their current accuracy [29, 30, 32], PACE and EarthCARE observations contain enough information to constrain ERF

(Supplementary Fig. 2). The synthetic experiment also indicates that our constraint method (based on history matching) gives a more conservative uncertainty estimate.

For real observations, to investigate the effect of the combined constraint and individual constraints on ERF, ERF_{aci}, and ERF_{ari}, Fig. 1 shows the prior and posterior ERF probability density functions (PDFs) with their uncertainty ranges (90% credible intervals). The combined observational constraint causes a more negative ERF than the unconstrained PPE (mean shift from -1.12 W m^{-2} to -1.52 W m^{-2}). The 90% confidence interval (CI) of the ERF is reduced by 0.46 W m^{-2} (34%), which primarily excludes the less negative values of the ERF distribution (above -0.9 W m^{-2}). For ERF_{aci}, the observational constraint tightens the distribution (reducing uncertainty by 0.38 W m^{-2} or 31%), and shifts it slightly less negative compared to the mean of the unconstrained PPE (Fig. 1), while for ERF_{ari}, there is a strong negative shift, due to spurious positive values being ruled out, as well as a strong reduction in uncertainty (0.77 W m^{-2} or 66% in CI range). Quantifying the effect of individual observational constraints gives insight into which observations have the strongest effect on the combined constraint. Here, AOD_{fine}, AI, and SSA have the largest effect on ERF uncertainty reduction. The remaining observations exert weaker constraints when applied individually, but still have a considerable effect in the combined constraint, as omitting any observation type results in a different posterior ERF distribution (not shown). All individual constraints are consistent with one another in the sense that their uncertainty ranges overlap. The ERF_{aci} uncertainty reduction is driven by AOD_{fine} and AI, followed by f_{2km} and SSA (Fig. 1). The ERF_{ari} uncertainty reduction has clearly the strongest effect from SSA, followed by AOD_{fine}, AI, and f_{2km} (EarthCARE).

The negative shift in ERF is most prominent over mid-to-high latitude Northern Hemisphere, the Amazon, Northern Africa, and India, consistent with the largest

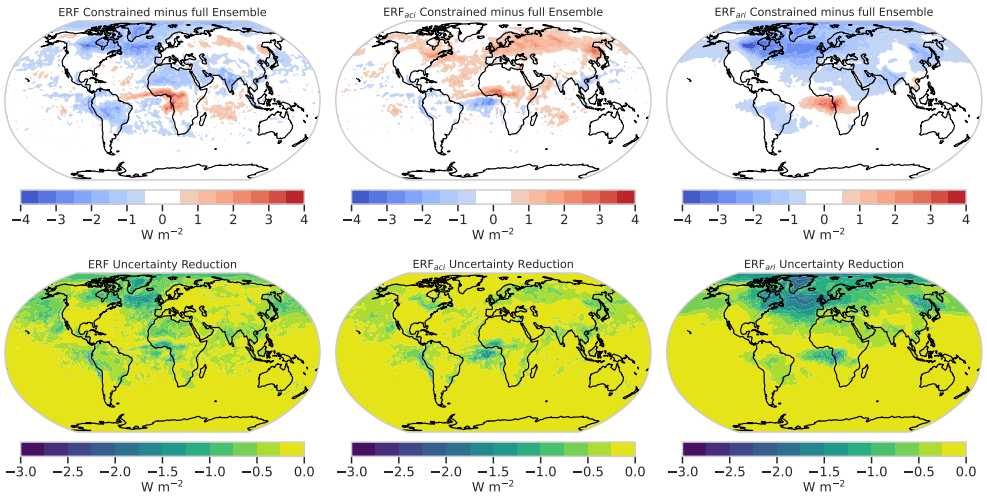


Fig. 2 Spatial distribution of the joint observational constraint on annual mean aerosol forcing. Top row shows the change in the ensemble mean (constrained minus unconstrained) for (left) total aerosol ERF, (middle) ERF$_{aci}$, and (right) ERF$_{ari}$. The bottom row shows the corresponding reduction in ensemble uncertainty (constrained minus unconstrained uncertainty) for each forcing. Negative values indicate decreased uncertainty under the joint constraint. See Supplementary Fig. 3 for the relative change in uncertainty.

uncertainty reductions (Fig. 2). A positive ERF shift is also evident over Equatorial Africa and its outflow regions. ERF$_{ari}$ shows overall similar shifts in the spatial pattern as ERF. The above-mentioned regions with the strongest shift in ERF correspond to regions with strong biomass burning emissions, suggesting that the constraint has a large effect on biomass burning emissions and properties. ERF$_{aci}$ has a different response to the constraint, with positive shifts in Eurasia, North America, and the Savannah, and negative shifts over the Tropical- Atlantic and Pacific oceans and South-East Asia. The spatial patterns in Fig. 2 reflect the combined influence of changes in Present-day (PD) - Pre-Industrial (PI) aerosol differences, aerosol absorption properties, and cloud droplet activation.

The constrained PPE yields a substantial reduction in annual mean uncertainty in the model equivalents of the observations, where the regional uncertainty range of the constrained PPE still overlaps with that of the observation (Fig. 3), relative to the variants with the strongest agreement across all observational constraints (See Constraint

Procedure in Methods). Fig. 3 shows that the constraint from each observational diagnostic mostly narrows the PPE closer toward the observation across each region. This indicates that the constrained PPE provides an ERF estimate that is consistent with the different observed aerosol and cloud properties over most regions, within the observational uncertainty. In most regions, the observations indicate a reduction in fine-mode aerosol ($\mathrm{AOD_{fine}}$, AI) and a consistent decrease in N_d (Fig. 3). An exception is the Savannah region, where observations suggest higher AI but lower N_d (Fig. 3), pointing to structural deficiencies in the representation of cloud condensation nuclei activity in biomass-burning aerosol or in the activation scheme. We also note that for N_d in many regions, the observational uncertainty is relatively large compared to the spread of the unconstrained ensemble.

There is overall spatial consistency in ERF shift between the applied individual constraints from $\mathrm{AOD_{fine}}$, SSA, AI, and N_d (Fig. 4; Supplementary Fig. 4 and Supplementary Fig. 5 show the ERF_{aci} and ERF_{ari}, respectively), where all show a similar negative shift in the northern hemisphere and a positive shift around Equatorial Africa. This suggests that these observations affect the same model parameters in a similar way. On the other hand, $\mathrm{AOD_{coarse}}$ and $\mathrm{f_{2km}}$ show spatial ERF shifts that are roughly consistent with each other but different from the other individual constraints. $\mathrm{AOD_{coarse}}$ and $\mathrm{f_{2km}}$ affect (mostly) different model parameters than the other observations (Fig. 5), which cause a different shift from the ERF PPE mean when applied individually. However, when combined with constraints from other observations, the changes across all parameter distributions result in a spatial ERF shift consistent with all observations within their uncertainty ranges. In contrast, individual constraints risk overfitting, resulting in a spatial ERF shift that is only self-consistent with a single observational diagnostic. Finding a combined constraint consistent with many

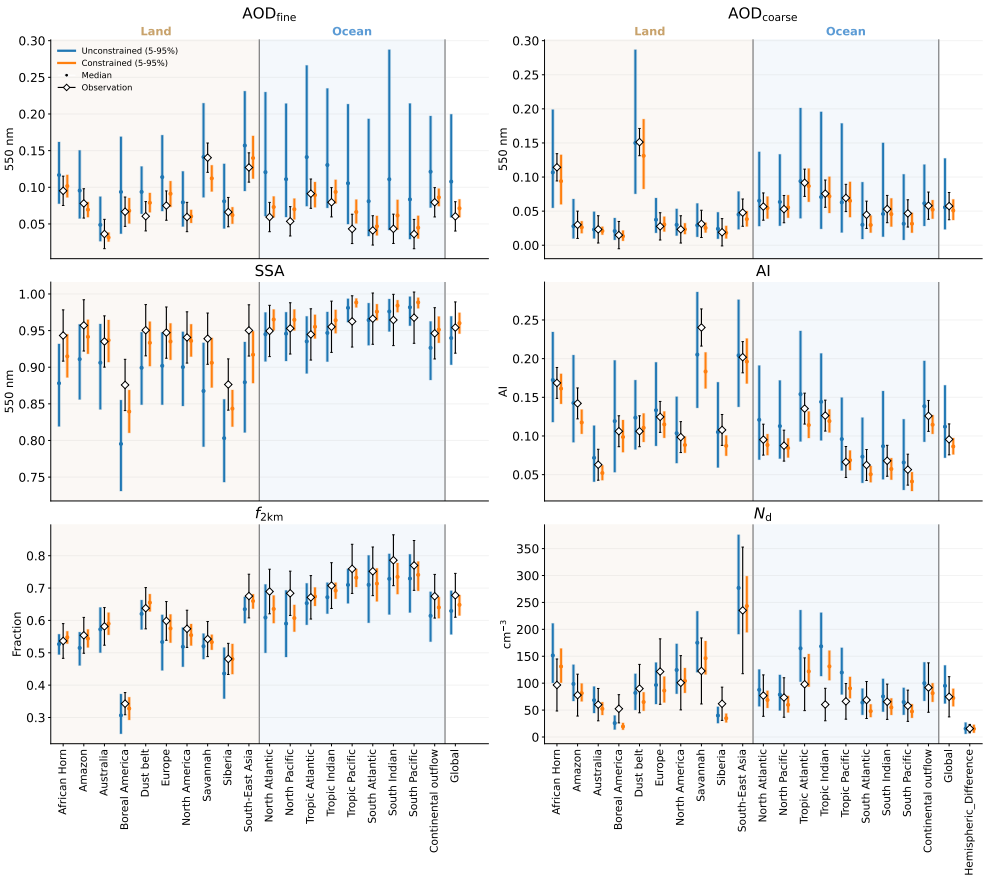


Fig. 3 Regional distributions of each observational diagnostic in the emulated PPE before and after applying the combined constraint. Blue intervals show the 5-95% range of the unconstrained ensemble and orange intervals the 5-95% range of the constrained ensemble; dots mark the medians. White diamonds show the regional observations, with error bars indicating the tolerance used in the constraint (Supplementary Table 2). Regions are grouped into land (left) and ocean (right), followed by the global mean; for N_d, the hemispheric difference is also shown. Panels show AOD_{fine} (550 nm), AOD_{coarse} (550 nm), SSA (550 nm), the aerosol index (AI, dimensionless), the fraction of aerosol extinction below 2 km (f_{2km}), and cloud droplet number concentration (N_d; cm^{-3}).

observations contrasts with earlier studies that reported conflicts among older satellite and/or ground-based constraints, which observational errors or model structural deficiencies may drive [7, 8, 10].

Constraints on processes, aerosol emissions, and properties

We quantify how model parameter distributions (mean and range, Supplementary Fig. 6) are modified by the combined observational constraint and by individual observational constraints (Fig. 4, Fig. 5). See Supplementary Table 1 for a description of each parameter perturbed.

SSA provides the most direct constraint on absorption and pushes the imaginary refractive indices of black carbon (BC), organic carbon (OC), and dust toward less absorbing values (Fig. 5), producing a large ERF_{ari} response when applied alone (Supplementary Fig. 5). Consistent with the SSA constraint, AI and $\mathrm{f_{2km}}$ also shift OC refractive indices to smaller values, indicating that PPE members matching fine-mode optical information and aerosol vertical placement also tend to be less absorbing. There is also a clear systematic constraint on the sources of marine aerosols. Across $\mathrm{AOD_{fine}}$, AI, $\mathrm{f_{2km}}$, and N_d observations, the posterior shifts toward reduced fine-mode marine aerosol (Fig. 3) through decreased DMS and fine sea-salt emissions (Fig. 5), a signal retained under the joint constraint. The combined constraint results in an increase of some aerosol removal parameters, including in-cloud wet-deposition, driven by $\mathrm{AOD_{fine}}$, AI, and especially $\mathrm{f_{2km}}$ (Fig. 5). For dry deposition of accumulation mode aerosol, there is a slight negative shift driven by $\mathrm{AOD_{fine}}$ and AI. The sulfate coating thickness is constrained towards lower values by both $\mathrm{AOD_{coarse}}$ and $\mathrm{f_{2km}}$, while SSA indicates a positive shift, resulting in a moderate reduction in the combined constraint.

Both $\mathrm{f_{2km}}$ (EarthCARE) and $\mathrm{AOD_{coarse}}$ also provide unique constraints on certain parameters. $\mathrm{f_{2km}}$ provides a constraint on the vertical distribution of aerosol that complements spatial ERF patterns of other observations (Fig. 4), which prevents other observational constraints from reproducing a correct column burden by compensating with unrealistic lifetimes or vertical placement. By constraining where aerosol resides in the column, it also provides a unique constraint on SO_2 oxidation, possibly as a proxy for aerosol lifetime (Fig. 5). Coarse-mode information isolates distinct

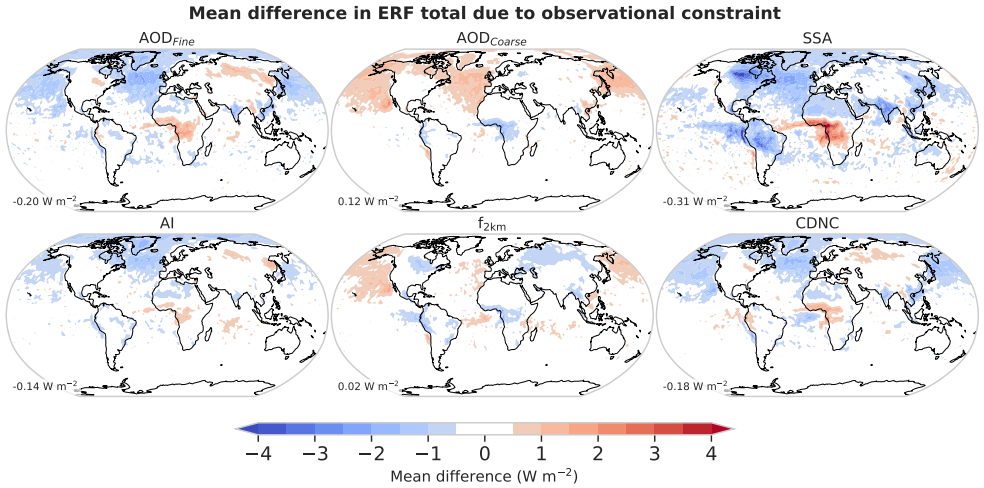


Fig. 4 Same as the top panel in Fig. 2 but showing the regional forcing response to observational constraints applied independently. Columns correspond to the individual constraints (AOD_{fine}, AOD_{coarse}, SSA, AI, f_{2km}, N_d). The difference represents the constrained minus unconstrained ensemble-mean difference in total aerosol ERF. The annotated value in each panel shows the global annual-mean change for that constraint (W m^{-2}).

source controls on dust and coarse sea salt, resulting in a robust constraint on the friction velocity threshold for dust emission and shifting the wind-speed dependence of coarse sea-salt emissions (Fig. 5). While these constraints are physically targeted and robust at the parameter level, their global-mean forcing uncertainty reduction is lower than that of AOD_{fine} and AI (Fig. 1). Therefore, ERF is mainly driven by fine-mode aerosols, because the model's PI and PD dust emissions are virtually the same in this model. In reality, dust emissions may have changed since the pre-industrial period due to land-use and climate changes [33], so the contribution of dust to ERF may be underestimated by this design.

Biomass-burning OC emissions are consistently pulled toward lower values by AOD_{fine}, AI, and N_d, but SSA and f_{2km} push the parameter to higher emissions, with only marginally overlapping uncertainty ranges (Fig. 5). These apparent conflicts highlight where multiple compensating pathways in the model can satisfy a single observable, especially for intrinsic aerosol properties (SSA and f_{2km}) that provide no

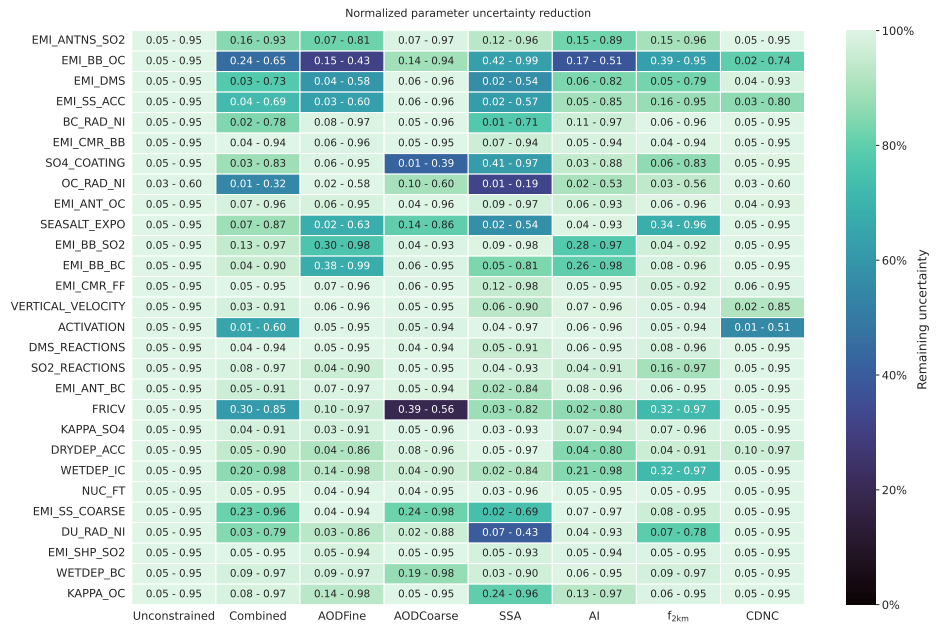


Fig. 5 Constraint-induced changes in parameter uncertainty relative to the full PPE. Colors indicate the remaining normalized parameter uncertainty after constraint, defined as the constrained 5-95% normalized parameter range by the corresponding 5-95% normalized range of the full PPE, where 100% denotes no constraint in uncertainty. Parameters are ordered (top to bottom) by their relative contribution to ERF uncertainty (See Supplementary Fig. 7). Numbers within each cell show the constrained 5th and 95th percentile parameter values. Columns show the combined joint constraint and the individual observational constraints (AODfine, AODcoarse, Single Scattering Albedo (SSA), Aerosol Index (AI), fraction of aerosol below 2 km (f_{2km}), and cloud droplet number concentration (N_d)).

information on aerosol burden. These apparent inconsistencies are a sign of overfitting in some of the individual constraints, whereas the combined constraint indicates there is a posterior PDF that is in line with all observations within their uncertainties (Fig. 3). On the other hand, the combined constraint is somewhat looser on some parameters than what would have been obtained by an 'optimal' subset of observations [8, 34]. Finally, observed N_d provides a unique sharp constraint on activation fraction and, to a lesser extent, vertical velocity (Fig. 5), which can have a large impact on ERF_{aci} in some models [19, 35], although it does not dominate overall uncertainty for the ECHAM6-HAM PPE [4].

Discussion and implications

Our results suggest that improved observational capability might reduce parametric equifinality in the PPE by constraining shared, ERF-relevant degrees of freedom, resulting in an ERF estimate that is consistent across observation types [12, 14]. Equifinality arises when a constraint matches a certain set of observations due to compensating errors [14]. By predominantly using satellite products that directly measure aerosols, in addition to commonly used N_d observations, we obtain a strong ERF constraint (Fig. 1). Because aerosol properties directly control both radiative effects and cloud-relevant quantities, constraining aerosol processes is necessary before interpreting cloud responses. Without this, cloud-based constraints alone may favor parameter combinations that reproduce cloud properties for the wrong physical reasons, which may result in equifinality [12].

We show that ERF uncertainty is reduced by 0.46 W m $^{-2}$ (34%) for a combined constraint using 6 different observables for 12 months and 18 regions. The strongest ERF constraint comes from Biomass Burning emissions and aerosol absorption properties, and an equal contribution from natural and anthropogenic emissions (Supplementary Fig. 8). Most individual constraints reduce DMS and fine-mode sea-salt emissions relative to the unconstrained ensemble mean (Fig. 5 and Supplementary Fig. 6), reducing the marine fine-mode aerosol background. As natural marine sulfur emissions dominate the natural aerosol background in remote regions [4, 5, 11, 21, 36, 37], changes in DMS and sea-salt emissions directly influence the PI aerosol concentration against which anthropogenic perturbations are measured [1, 38]. A reduction in the pre-industrial marine aerosol background increases the PD-PI contrast in aerosols and strengthens aerosol forcing [38, 39].

The strongest impact of the combined constraint is on ERF_{ari}, which undergoes both a considerable negative shift and the largest uncertainty reduction of 66% (unconstrained range of 1.16 W m $^{-2}$ to a constrained range of 0.39 W m $^{-2}$). The ERF_{ari}

in the full PPE has a large uncertainty, mostly related to biomass burning absorption properties of BC and OC (Supplementary Fig. 7), consistent with PPEs of other models [8]. The tight ERF_{ari} constraint, with a new mean of -0.1 W m $^{-2}$, is primarily due to the constraint on aerosol absorption that strongly influences radiative efficiency [40, 41]. Multiple constraints favor weaker absorption by black carbon and organic carbon, which turns a positive ERF_{ari} into a negative one, similar to earlier findings that suggest aerosols in most climate models are too absorbing [42, 43]. It is important to note that the period used for this study (August 2024 - July 2025) was affected by intense biomass-burning events, especially in Canada and South America [44], which may contribute to the high uncertainty in biomass-burning aerosol properties and positive ERF_{ari} during this period.

In contrast to ERF_{ari}, ERF_{aci} exhibits a mean shift towards less negative values (from -1.56 to -1.44 W m $^{-2}$) and narrows in uncertainty by 0.38 W m $^{-2}$ (31%) under the combined constraint. Substantial uncertainty persists in aerosol-cloud interaction components, which could partly be attributed to structural model deficiencies. Unlike in some other models, where updraft velocity is among the largest contributors to ERF_{aci} uncertainty [19, 35], vertical velocity and the activation parameter contribute little to ERF_{aci} uncertainty in ECHAM6-HAM (Supplementary Fig. 7). As a result, although N_d provides a sharp constraint on the activation parameter, this does not translate into a substantial reduction in ERF_{aci} uncertainty. Anthropogenic SO_2 and DMS emissions remain among the largest contributors to ERF uncertainty from ACI (Supplementary Fig. 8) even after applying observational constraints. This is likely due to the use of a single global scaling factor, which cannot capture spatial and temporal variability in sulfur emissions or the regional dependence of their atmospheric processing and transport [8, 10, 45]. Also, natural marine sulfur emissions from DMS remain an important cause of remaining ERF_{aci} uncertainty (Supplementary Fig. 8 and Supplementary Fig. 7), as remaining uncertainties probably relate to structural

model uncertainties from both oceanic DMS concentrations and marine sulfur chemistry [11, 37, 46]. On the other hand, the current set of observations does not provide a constraint on the emitted particle size of fossil fuel and biomass burning emissions, which contributes substantially to the remaining ERF_{aci} uncertainty (Supplementary Fig. 8). Here, additional use of in-situ observations of ultra-fine particles may help to achieve a stronger constraint.

A next step would be to constrain ERF across different aerosol-climate models. If ERF within a single model can be coherently constrained across multiple regions (Fig. 3) using a variety of observations, this increases confidence that the constrained response is not solely dependent on regional compensating biases or specific parameter choices. Extending similar constraints to a coordinated multi-model PPE framework [4, 14, 15] would allow the relative roles of parametric and structural uncertainty in ERF to be assessed more directly. Convergence toward overlapping ERF estimates under a common observational constraint would suggest that part of the present inter-model spread arises from unconstrained parameter choices, whereas persistent differences would indicate a larger role for structural model differences. Such an approach would also help identify which aerosol processes are consistently constrained across models and which remain model-dependent [47]. Spatially coherent parameter constraints across independent observations may further support emergent-constraint approaches by reducing susceptibility to compensating regional biases [48]. Testing this will require expanded PPE coverage across models and additional observation types [2, 47].

To conclude, satellite retrievals from the Plankton, Aerosol, Cloud and ocean Ecosystem (PACE) and Earth Cloud, Aerosol, and Radiation Explorer (EarthCARE) provide high-quality observations that enable observationally consistent constraints across different observables, resulting in a considerable reduction in ERF uncertainty.

Independent constraints on fine- and coarse AOD, AI, N_d, and $f_{2\mathrm{km}}$ converge on overlapping posterior parameter distributions and a coherent ERF response (Fig. 1, Fig. 3). The fact that we find a constrained set of parameters that are consistent with many different observations individually contrasts with earlier multi-constraint studies in which additional observations often led to incompatible parameter adjustments, limiting uncertainty reduction [8–10]. Our constrained ERF of -1.5 [-2 to -1.1] W m $^{-2}$ lies within the IPCC AR6 range of -2.0 to -0.6 W m^{-2}, but is more negative than the AR6 best estimate of -1.3 W m^{-2} [1]. The AR6 assessment combines multiple avenues including satellite-based observational estimates (-1.4 [-2.2 to -0.6] W m^{-2}), and climate model-based estimates (-1.25 [-2.1 to -0.4] W m^{-2}) [1, 31, 49]. Interestingly, our ERF estimate is closer to the satellite-based observational evidence than CMIP6. Also, the constrained $\mathrm{ERF}_{\mathrm{aci}}$ is in line with recent observational evidence of strong cooling due to ACI [50–52]. The remaining uncertainty highlights processes that are poorly constrained, including regional emissions variability and aerosol microphysical processing. Further progress will likely depend on improved regional emission constraints from data assimilation, advances in process representation, and combining satellite with in-situ constraints.

Materials and Methods

Model Configuration

We use the ECHAM6.3-HAM2.3 aerosol-climate model (referred to here as "ECHAM6-HAM"), configured following Neubauer et al. [23] and Tegen et al. [24].

Simulations are performed for August 2024 to July 2025, matching the period of the PACE and EarthCARE observations. The model is nudged towards the ERA5 reanalysis [53] using the standard ECHAM6 nudging configuration [24, 54], in which vorticity, divergence and surface pressure are relaxed towards the reanalysis with relaxation timescales of 6 h, 48 h and 24 h, respectively. Sea surface temperature and sea ice

concentration are prescribed from ERA5 monthly means for the same period. The pre-industrial simulations use identical nudging and the same sea surface temperature and sea ice boundary conditions, differing from the present-day simulations only in their aerosol and precursor emissions, so that effective radiative forcing (ERF) is diagnosed as the difference in top-of-atmosphere radiative fluxes under the same meteorology. PI simulations use CEDS anthropogenic and CMIP6 biomass-burning emissions [55, 56] representative of 1850, while PD simulations use CEDS anthropogenic emissions and GFAS CAMS biomass-burning emissions representative of 2024 and 2025 [55, 57].

Aerosol ERF and its components are calculated following the diagnostic approach of Ghan et al. [58]. See Supplementary Note 1 for more information on this calculation.

Satellite Observations

This study uses measurements taken onboard NASA's Plankton, Aerosol, Cloud and ocean Ecosystem (PACE) [25], launched February 2024, and ESA's Earth Cloud, Aerosol, and Radiation Explorer (EarthCARE) [27], launched May 2024.

PACE

We use aerosol observations AOD_{fine}, AOD_{coarse}, AI, and SSA from SPEXone [26, 28] on PACE. SPEXone measures intensity and polarization in the range 385-770 nm at 5 viewing angles for 5.2 $\times$5.2 km pixels within a 100 km swath. Aerosol retrievals from SPEXone are performed using the Remote sensing of Trace gas and Aerosol Products (RemoTAP) algorithm [28, 59]. RemoTAP retrieves aerosol properties (effective radius, effective variance, refractive index, column number) in three log-normal modes, made up of one fine mode and two coarse modes (insoluble and soluble). Subsequently, aerosol optical properties (AOD_{fine}, AOD_{coarse}, AI (aerosol index, the product of AOD and Angstrom Exponent), and SSA) are computed, as used in this study. SPEXone has demonstrated high-quality agreement with AERONET [28].

In addition to SPEXone aerosol observations, we also use N_d observations from OCI on PACE. OCI is a spectrometer, providing hyperspectral observations from the ultraviolet (315 nm) to the near-infrared (895 nm). In addition, OCI includes discrete shortwave infrared bands centered at 940, 1038, 1250, 1378, 1615, 2130, and 2260 nm. OCI cloud retrievals employ the bi-spectral approach to retrieve liquid cloud effective radius (CER) and cloud optical thickness (COT), as described in Nakajima and King [60] and Platnick et al. [61]. Subsequently, N_d is computed using the approach of Grosvenor et al [62].

EarthCARE

Aerosol extinction coefficients are obtained from the Level 2 low-resolution extinction, backscatter, and depolarization products (A-EBD), along with the associated target classification (A-TC) products that classify features into aerosols (sea salt, dust, smoke, continental pollution, stratospheric aerosols), clouds (liquid and ice), and clear sky conditions [63–65]. The retrieved data are filtered using the following criteria: 1) data with a good quality flag are kept, 2) features classified as aerosols are used, 3) extinction coefficients with low signal-to-noise ratio and features classified as clear-sky are set to zero, and 4) data classified as ice clouds, below-surface, negative extinction coefficients, or columns with full attenuation and liquid clouds are removed from the dataset. Vertical coordinates have been converted from altitude above WGS84 (World Geodetic System 1984) ellipsoid to altitude above EGM96 (Earth Gravitational Model 1996), which approximates mean sea level. After filtering, the extinction coefficients are vertically interpolated to uniform altitude levels. The filtered and interpolated extinction coefficient and surface elevation data are then gridded to daily 2° resolution by calculating the mean value for each vertical level within each 2° grid cell. The number of valid extinction coefficients and standard deviations in each 2° grid cell are also calculated to ensure the sampled data are representative.

To effectively identify the proportion of aerosol above and below the boundary layer, we use the fraction of aerosol below 2 km, referred to as f_{2km}. f_{2km} is defined as the fraction of the total column aerosol extinction (integrated between 0–40 km) that occurs below 2 km altitude, calculated identically from model output and EarthCARE/ATLID retrievals as the ratio of vertically-integrated extinction below 2 km to that integrated over the full 0–40 km column.

Perturbed Parameter Ensemble

Each simulation had a 4-month spin-up phase, which was removed from the analysis. We perturbed 28 aerosol and physical atmosphere parameters (Supplementary Table 1) across 250 simulations for Present-day and Pre-industrial (8.9 ratio of ensemble size to number of parameters), excluding the control run, expanding on the previous ECHAM6-HAM PPE [4]. Each parameter range reflects the uncertainty in the associated physical process determined from expert elicitation. For a more detailed description of PPEs, including the model, see Bhatti et al. [4].

Constraint Procedure

We co-locate each model diagnostic with each observational pair in space and time [18, 66], such as modeled AOD_{fine} with the corresponding AOD_{fine} observation (See Supplementary Table 2). For example, AOD_{fine} is measured on board the PACE satellite using the SPEXone instrument, which has a swath of 100km with 5.2 $\times$ 5.2km ground pixels, regridded to 1 degree x 1 degree [28]. We then interpolate that diagnostic (AOD_{fine} (Aitken + Accumulation mode)) for all PPE variants to the observations every 3 hours. Once co-located, all data arrays are aggregated over 12 months.

We apply a Gaussian process (GP) emulator using the Earth System Emulator package (ESEm; [67]). This choice follows recent guidance in PPE-based climate uncertainty studies [4, 13, 19]. GP emulators greatly reduce the computational cost and storage that would be required to run an equivalent number of full model simulations,

while still supporting robust uncertainty and constraint quantification. The emulator is trained to predict 2 million monthly-mean fields at each model 96 × 192 grid cell, which are referred to as model variants. The emulator validation for all diagnostics is shown in Supplementary Fig. 9.

To constrain parametric uncertainty while reducing the influence of structural model deficiencies, we first identify regions where model-observation disagreement is unlikely to provide a meaningful parameter constraint, similar to earlier PPE constraint studies [10, 14, 19, 68, 69]. For each observational diagnostic, grid cells where the model output falls persistently outside observational uncertainty bounds are excluded from subsequent analysis (Supplementary Table 2). These rejected grid cells (Supplementary Fig. 10 and Supplementary Fig. 11) are interpreted as regions where structural model error, representativeness limitations, or unresolved observational inconsistencies dominate the mismatch [10]. For N_d, we additionally include the hemispheric contrast, ΔN_d, defined as the difference between the mean N_d (ocean-only) in the Northern and Southern Hemispheres [20]. ΔN_d is treated as an additional target region in the N_d cost function.

Following this filtering step, the retained grid cells with monthly mean observations are aggregated into 19 physically distinct regions representing different aerosol and cloud regimes (Supplementary Fig. 1). For each of the 2 million PPE variants, monthly regional co-located means are computed for all six observational diagnostics, allowing a one-to-one comparison between simulated and observed regional-monthly behavior. In addition, the N_d diagnostic includes a hemispheric contrast metric (ΔN_d) following McCoy et al. [20]. The justification for including a continental outflow region is shown in Supplementary Fig. 12. Altogether, this results in a total of 1378 regional-monthly observations to be used for the constraint.

Model variants are evaluated using a multivariate least-squares cost function. For each PPE variant, k, the cost function for each observable v is defined as

$$\chi^2_{\nu,k} = \frac{1}{N_\nu} \sum_{i=1}^{N_\nu} \left(\frac{M_{\nu,k,i} - O_{\nu,i}}{\sigma_{\nu,i}} \right)^2 \quad (1)$$

where $M_{\upsilon,k,i}$ is the simulated regional-monthly diagnostic for PPE variant k, $O_{\upsilon,i}$ is the corresponding observation, $\sigma_{\upsilon,i}$ is the prescribed uncertainty tolerance shown in Supplementary Table 2, i indexes the retained regional-monthly observational elements for observable υ, and N_υ is the total number of such elements.

The uncertainty tolerances (from Supplementary Table 2) $\sigma_{\upsilon,i}$ combine observational uncertainty with uncertainty related to representation differences between model and observations at the regional scale, as well as emulator uncertainty. Error tolerances were taken from satellite- and instrument-specific expert elicitation.

A joint cost is then defined as the N_υ-weighted mean across all diagnostics,

$$\chi^2_{\text{joint},k} = \frac{\sum_\nu N_\nu \, \chi^2_{\nu,k}}{\sum_\nu N_\nu} \quad (2)$$

which is equivalent to computing a single value over all N_{tot} observational constraints simultaneously. Model variants are only retained or 'chosen' if:

$$\chi^2_{\text{joint}} \leq f \, \chi^2_{\text{min}} \quad (3)$$

where χ^2_{min} is the minimum joint cost across the PPE. By defining the maximum acceptable χ^2 relative to χ^2_{min} we effectively normalize χ^2_{min}, and we can relate f to confidence limits of the χ^2 probability distribution [70]. If all 1378 measurements were independent, then $f = 1.06$ would represent the 95^{th} percentile of the reduced χ^2 distribution [70]. However, this threshold would result in only a few tens of PPE members being selected, and it is not realistic to assume that all observations are independent. For $f = 1.3$, a sufficiently large subset of PPE members (1290) is retained to construct a posterior distribution. This value of f corresponds approximately to the 95^{th} percentile of the reduced χ^2 distribution assuming 70 independent observations. This

should be interpreted as a deliberately conservative assumption regarding the effective number of independent observations, since it implies roughly one independent observation per twenty measurements. In practice, the effective number of independent observations is likely larger than 70 due to correlations being weaker than this conservative estimate, which would correspond to a narrower $\chi^2_{\min}$ distribution and therefore a smaller admissible range for $\chi^2_{\min}$. Nevertheless, we choose not to reduce f, as doing so would lead to an unacceptably small ensemble size for constructing robust posterior statistics. On the other hand, it is important to note that results do not change drastically when increasing f to 1.4 (ERF range would become -2.0 to -1.05 W m $^{-2}$ with 3982 members selected).

An emulator validation assesses how many original PPE members lie within the accepted parameter space (Supplementary Fig. 13). We applied the same cost function and acceptance threshold to the simulated output of the 251 PPE members (Supplementary Fig. 13). One PPE member satisfies the constraint, and a further 11 lie within 1.5 times the threshold. This is consistent with the accepted range (1290) occupying 0.065% of the prior parameter space (2 million), in which fewer than one of the 251 members would be expected. The cost distribution of the PPE members closely follows that of the emulated samples, shown in Supplementary Fig. 13, indicating that the emulators reproduce the model's agreement with observations across the ensemble. Additionally, the simulated ERF of the two best-fitting PPE members from the training data set (-1.34 and -1.54 W m $^{-2}$) lies within the constrained 5-95% range (-1.97 to -1.07 W m $^{-2}$), providing an emulator-independent consistency check of the constrained ERF. Together with the emulator validation results (Supplementary Fig. 9) indicates that the emulator uncertainty in the accepted range is modest.

The retained subset should be interpreted as a comparatively well-constrained region of parameter space rather than a quantitatively non-implausible set in the strict history-matching methodology [14, 69]. In total, 1290 of the 2 million model variants

satisfy the joint constraint criterion. Individual observational constraints are imposed by applying the same criterion to each individual cost function ($\chi^2_{v,k}$), thereby enabling identification of observation-specific constraint behavior.

Synthetic Experiment

We randomly selected 500 model variants from the emulated ensemble and treated them as the truth. Synthetic observations of all six observables were generated from the truth's emulated regional-monthly values, with added noise whose standard deviations equal the tolerances in Supplementary Table 2. Although there are indications of correlations between different months and regions, to be on the conservative side, we also imposed a correlation between months of $0.5^{d-1)}$, where d is the distance in months, and a correlation of 0.3 between adjacent regions. The constraint (Equations (1)-(3)) was then applied, and the result (median of constrained distribution and 5-95 percentile range) was then compared against the known truth.

Acknowledgments

We thank all data producers for making the satellite data and input data available. YB, HJ, UI, AN, BD, and OH are supported by the EU Horizon 2020 project CleanCloud (grant no. GA 101137639). Computational resources were provided by the Dutch national e-infrastructure with computing resources provided by SURF Cooperative (grant no. EINF-11775, EINF-8447, NWO-2025.001).

Author contributions:

Writing–original draft: Y.B Conceptualization: Y.B, H.J., O.H., B.v.D., N.S., A.N., C.S., and U.I. Investigation: Y.B., H.J., O.H., and L.R. Writing–review and editing: Y.B, L.R., O.H., B.v.D., N.S., X.W. Methodology: Y.B., H.J., L.R., N.S., D.W.P., and O.H. Resources: H.J., O.H., A.A., X.W., G.F., and G.V.Z., Funding acquisition: Y.B., H.J., and O.H. Data curation: Y.B., G.F., O.H., X.W., and G.V.Z. Formal analysis:

Y.B., H.J., O.H., N.S., and L.R. Software: Y.B., and D.W.P. Project administration: Y.B., and O.H. Visualization: Y.B.

Competing interests:

The authors declare no competing interests

Data availability:

Raw PACE observations can be found in https://pace.oceansciences.org/data.htm and EarthCARE observations can be found in https://earth.esa.int/eogateway/missions/earthcare/data. To access post-processed EarthCARE or PACE observations (such as f_{2km}), or for higher frequency PPE data (monthly, daily, 3-hourly) or additional PPE diagnostics, please contact the corresponding author.

Code availability:

The ECHAM6-HAM model source code can be accessed in Redmine from https://redmine.hammoz.ethz.ch. The ESEm code used to emulate the simulations is in https://doi.org/10.5281/zenodo.5466563 [67].

References

[1] Forster, P. *et al.* in *The Earth's energy budget, climate feedbacks, and climate sensitivity* (eds Masson-Delmotte, V. *et al.*) *Climate Change 2021: The Physical Science Basis. Contribution of Working Group I to the Sixth Assessment Report of the Intergovernmental Panel on Climate Change* 923–1054 (Cambridge University Press, Cambridge, United Kingdom and New York, NY, USA, 2021).

[2] Bellouin, N. *et al.* Bounding Global Aerosol Radiative Forcing of Climate Change. *Reviews of Geophysics* **58**, e2019RG000660 (2020). URL https://doi.org/10.1029/2019RG000660.

[3] Twomey, S. Pollution and the planetary albedo. *Atmospheric Environment (1967)* **8**, 1251–1256 (1974). URL https://www.sciencedirect.com/science/article/pii/0004698174900043.

[4] Bhatti, Y. A. *et al.* Uncertainty in aerosol effective radiative forcing from anthropogenic and natural aerosol parameters in ECHAM6.3-HAM2.3. *Atmospheric Chemistry and Physics* **26**, 269–293 (2026). URL https://acp.copernicus.org/articles/26/269/2026/.

[5] Yoshioka, M. *et al.* Ensembles of Global Climate Model Variants Designed for the Quantification and Constraint of Uncertainty in Aerosols and Their Radiative Forcing. *Journal of Advances in Modeling Earth Systems* **11**, 3728–3754 (2019). URL https://onlinelibrary.wiley.com/doi/abs/10.1029/2019MS001628.

[6] Gliß, J. *et al.* AeroCom phase III multi-model evaluation of the aerosol life cycle and optical properties using ground- and space-based remote sensing as well as surface in situ observations. *Atmospheric Chemistry and Physics* **21**, 87–128 (2021). URL https://acp.copernicus.org/articles/21/87/2021/.

[7] Prévost, L. M. C. *et al.* Detection of potential structural deficiencies in a global aerosol model using a perturbed parameter ensemble. *Atmospheric Chemistry and Physics* **26**, 2487–2530 (2026). URL https://acp.copernicus.org/articles/26/2487/2026/.

[8] Regayre, L. A. *et al.* Identifying climate model structural inconsistencies allows for tight constraint of aerosol radiative forcing. *Atmospheric Chemistry and Physics* **23**, 8749–8768 (2023). URL https://acp.copernicus.org/articles/23/8749/2023/.

[9] Watson-Parris, D. *et al.* Constraining Uncertainty in Aerosol Direct Forcing. *Geophysical Research Letters* **47**, e2020GL087141 (2020). URL https://onlinelibrary.

wiley.com/doi/abs/10.1029/2020GL087141.

[10] Johnson, J. S. *et al.* Robust observational constraint of uncertain aerosol processes and emissions in a climate model and the effect on aerosol radiative forcing. *Atmospheric Chemistry and Physics* **20**, 9491–9524 (2020). URL https://acp.copernicus.org/articles/20/9491/2020/.

[11] Carslaw, K. S. *et al.* Large contribution of natural aerosols to uncertainty in indirect forcing. *Nature* **503**, 67–71 (2013).

[12] Lee, L. A., Reddington, C. L. & Carslaw, K. S. On the relationship between aerosol model uncertainty and radiative forcing uncertainty. *Proceedings of the National Academy of Sciences* **113**, 5820–5827 (2016). URL https://www.pnas.org/doi/10.1073/pnas.1507050113.

[13] Eidhammer, T. *et al.* An extensible perturbed parameter ensemble for the Community Atmosphere Model version 6. *Geoscientific Model Development* **17**, 7835–7853 (2024). URL https://gmd.copernicus.org/articles/17/7835/2024/.

[14] Carslaw, K. S. *et al.* Opinion: The importance and future development of perturbed parameter ensembles in climate and atmospheric science. *Atmospheric Chemistry and Physics* **26**, 4651–4667 (2026). URL https://acp.copernicus.org/articles/26/4651/2026/.

[15] Jia, H. *et al.* Process-level contributions to uncertainty in aerosol effective radiative forcing: a perturbed parameter ensemble with the aerosol–climate model ICON-HAM. *EGUsphere* 1–50 (2026). URL https://egusphere.copernicus.org/preprints/2026/egusphere-2026-3275/.

[16] Schutgens, N. *et al.* On the spatio-temporal representativeness of observations. *Atmospheric Chemistry and Physics* **17**, 9761–9780 (2017). URL https://acp.

copernicus.org/articles/17/9761/2017/.

[17] Ma, P.-L., Rasch, P. J., Chepfer, H., Winker, D. M. & Ghan, S. J. Observational constraint on cloud susceptibility weakened by aerosol retrieval limitations. *Nature Communications* **9**, 2640 (2018). URL https://www.nature.com/articles/s41467-018-05028-4.

[18] Schutgens, N. A. J. *et al.* Will a perfect model agree with perfect observations? The impact of spatial sampling. *Atmospheric Chemistry and Physics* **16**, 6335–6353 (2016). URL https://acp.copernicus.org/articles/16/6335/2016/.

[19] Regayre, L. A. *et al.* Aerosol and physical atmosphere model parameters are both important sources of uncertainty in aerosol ERF. *Atmospheric Chemistry and Physics* **18**, 9975–10006 (2018). URL https://acp.copernicus.org/articles/18/9975/2018/.

[20] McCoy, I. L. *et al.* The hemispheric contrast in cloud microphysical properties constrains aerosol forcing. *Proc Natl Acad Sci U S A* **117**, 18998–19006 (2020).

[21] Regayre, L. A. *et al.* The value of remote marine aerosol measurements for constraining radiative forcing uncertainty. *Atmospheric Chemistry and Physics* **20**, 10063–10072 (2020). URL https://acp.copernicus.org/articles/20/10063/2020/.

[22] Song, C. *et al.* Aircraft in-situ measurements from SOCRATES constrain the anthropogenic perturbations of cloud droplet number. *Atmospheric Chemistry and Physics* **25**, 16063–16083 (2025). URL https://acp.copernicus.org/articles/25/16063/2025/.

[23] Neubauer, D. *et al.* The global aerosol–climate model ECHAM6.3–HAM2.3 – Part 2: Cloud evaluation, aerosol radiative forcing, and climate sensitivity. *Geoscientific Model Development* **12**, 3609–3639 (2019). URL https://gmd.copernicus.

org/articles/12/3609/2019/.

[24] Tegen, I. *et al.* The global aerosol–climate model ECHAM6.3–HAM2.3 – Part 1: Aerosol evaluation. *Geoscientific Model Development* **12**, 1643–1677 (2019). URL https://gmd.copernicus.org/articles/12/1643/2019/.

[25] Werdell, P. J. *et al.* The Plankton, Aerosol, Cloud, Ocean Ecosystem Mission: Status, Science, Advances. *Bulletin of the American Meteorological Society* **96** (2019). URL https://journals.ametsoc.org/view/journals/bams/100/9/bams-d-18-0056.1.xml.

[26] Hasekamp, O. P. *et al.* Aerosol measurements by SPEXone on the NASA PACE mission: expected retrieval capabilities. *Journal of Quantitative Spectroscopy and Radiative Transfer* **227**, 170–184 (2019). URL https://www.sciencedirect.com/science/article/pii/S0022407318308653.

[27] Illingworth, A. J. *et al.* The EarthCARE Satellite: The Next Step Forward in Global Measurements of Clouds, Aerosols, Precipitation, and Radiation. *Bulletin of the American Meteorological Society* **96** (2015). URL https://journals.ametsoc.org/view/journals/bams/96/8/bams-d-12-00227.1.xml.

[28] Fu, G. *et al.* Aerosol Retrievals From SPEXone on the NASA PACE Mission: First Results and Validation. *Geophysical Research Letters* **52**, e2024GL113525 (2025). URL https://onlinelibrary.wiley.com/doi/abs/10.1029/2024GL113525.

[29] Fu, G., Lu, S., Gao, M., Rietjens, J. & Hasekamp, O. Collaborative Neural Networks Significantly Improve Global Aerosol Retrievals From Multiangle Polarimeters. *IEEE Transactions on Geoscience and Remote Sensing* **64**, 4107019–4107019 (2026). URL https://ieeexplore.ieee.org/abstract/document/11488611.

[30] Baars, H. *et al.* Validation of EarthCARE/ATLID aerosol profiling products with ground-based PollyNET lidars – case studies. *Atmospheric Measurement Techniques* **19**, 3831–3864 (2026). URL https://amt.copernicus.org/articles/19/3831/2026/.

[31] Smith, C. J. *et al.* Effective radiative forcing and adjustments in CMIP6 models. *Atmospheric Chemistry and Physics* **20**, 9591–9618 (2020). URL https://acp.copernicus.org/articles/20/9591/2020/.

[32] Fu, G. *et al.* Aerosol retrievals from different polarimeters during the ACEPOL campaign using a common retrieval algorithm. *Atmospheric Measurement Techniques* **13**, 553–573 (2020). URL https://amt.copernicus.org/articles/13/553/2020/.

[33] Kok, J. F. *et al.* Mineral dust aerosol impacts on global climate and climate change. *Nature Reviews Earth & Environment* **4**, 71–86 (2023). URL https://www.nature.com/articles/s43017-022-00379-5.

[34] Regayre, L. A. *et al.* Remaining aerosol forcing uncertainty after observational constraint and the processes that cause it. *Atmospheric Chemistry and Physics* **26**, 2293–2317 (2026). URL https://acp.copernicus.org/articles/26/2293/2026/.

[35] Nugent, J. M. *et al.* Overview of the Nephele Perturbed Parameter Ensemble for Aerosol-Cloud Interactions in E3SMv3. *Journal of Advances in Modeling Earth Systems* **18**, e2025MS004989 (2026). URL https://onlinelibrary.wiley.com/doi/abs/10.1029/2025MS004989.

[36] Revell, L. E. *et al.* Atmosphere-Ocean Feedback From Wind-Driven Sea Spray Aerosol Production. *Geophysical Research Letters* **48**, e2020GL091900 (2021).

[37] Bhatti, Y. A. *et al.* The sensitivity of Southern Ocean atmospheric dimethyl sulfide (DMS) to modeled oceanic DMS concentrations and emissions. *Atmospheric Chemistry and Physics* **23**, 15181–15196 (2023). URL https://acp.copernicus.org/articles/23/15181/2023/.

[38] Carslaw, K. S. *et al.* Aerosols in the Pre-industrial Atmosphere. *Current Climate Change Reports* **3**, 1–15 (2017). URL https://doi.org/10.1007/s40641-017-0061-2.

[39] Hamilton, D. S. *et al.* Occurrence of pristine aerosol environments on a polluted planet. *Proc Natl Acad Sci U S A* **111**, 18466–71 (2014).

[40] Williams, A. I. L., Stier, P., Dagan, G. & Watson-Parris, D. Strong control of effective radiative forcing by the spatial pattern of absorbing aerosol. *Nature Climate Change* **12**, 735–742 (2022). URL https://www.nature.com/articles/s41558-022-01415-4.

[41] Lacagnina, C., Hasekamp, O. P. & Torres, O. Direct radiative effect of aerosols based on PARASOL and OMI satellite observations. *Journal of Geophysical Research: Atmospheres* **122**, 2366–2388 (2017). URL https://onlinelibrary.wiley.com/doi/abs/10.1002/2016JD025706.

[42] Brown, H. *et al.* Biomass burning aerosols in most climate models are too absorbing. *Nature Communications* **12**, 277 (2021). URL https://www.nature.com/articles/s41467-020-20482-9.

[43] Samset, B. H. *et al.* Aerosol Absorption: Progress Towards Global and Regional Constraints. *Current Climate Change Reports* **4**, 65–83 (2018). URL https://doi.org/10.1007/s40641-018-0091-4.

[44] Kelley, D. I. *et al.* State of Wildfires 2024–2025. *Earth System Science Data* **17**, 5377–5488 (2025). URL https://essd.copernicus.org/articles/17/5377/2025/.

[45] Smith, S. J. *et al.* Anthropogenic sulfur dioxide emissions: 1850–2005. *Atmospheric Chemistry and Physics* **11**, 1101–1116 (2011). URL https://acp.copernicus.org/articles/11/1101/2011/.

[46] Bhatti, Y. A. *et al.* Aerosol and Dimethyl Sulfide Sensitivity to Sulfate Chemistry Schemes. *Journal of Geophysical Research: Atmospheres* **129**, e2023JD040635 (2024). URL https://onlinelibrary.wiley.com/doi/abs/10.1029/2023JD040635.

[47] Schutgens, N. *et al.* AEROCOM and AEROSAT AAOD and SSA study – Part 1: Evaluation and intercomparison of satellite measurements. *Atmospheric Chemistry and Physics* **21**, 6895–6917 (2021). URL https://acp.copernicus.org/articles/21/6895/2021/.

[48] Nowack, P. & Watson-Parris, D. Opinion: Why all emergent constraints are wrong but some are useful – a machine learning perspective. *Atmospheric Chemistry and Physics* **25**, 2365–2384 (2025). URL https://acp.copernicus.org/articles/25/2365/2025/.

[49] Zelinka, M. D., Andrews, T., Forster, P. M. & Taylor, K. E. Quantifying components of aerosol-cloud-radiation interactions in climate models. *Journal of Geophysical Research: Atmospheres* **119**, 7599–7615 (2014). URL https://onlinelibrary.wiley.com/doi/abs/10.1002/2014JD021710.

[50] Hasekamp, O. P., Gryspeerdt, E. & Quaas, J. Analysis of polarimetric satellite measurements suggests stronger cooling due to aerosol-cloud interactions. *Nature Communications* **10**, 5405 (2019). URL https://www.nature.com/articles/s41467-019-13372-2.

[51] Virtanen, A. *et al.* High sensitivity of cloud formation to aerosol changes. *Nature Geoscience* **18**, 289–295 (2025). URL https://www.nature.com/articles/s41561-025-01662-y.

[52] Jia, H. *et al.* Optimal choice of proxy for cloud condensation nuclei reduces uncertainty in aerosol-cloud-climate forcing. *Science Advances* **12**, eaea4828 (2026). URL https://www.science.org/doi/10.1126/sciadv.aea4828.

[53] Hersbach, H. *et al.* The ERA5 global reanalysis. *Quarterly Journal of the Royal Meteorological Society* **146**, 1999–2049 (2020).

[54] Zhang, K. *et al.* The global aerosol-climate model ECHAM-HAM, version 2: sensitivity to improvements in process representations. *Atmospheric Chemistry and Physics* **12**, 8911–8949 (2012). URL https://acp.copernicus.org/articles/12/8911/2012/.

[55] McDuffie, E. E. *et al.* A global anthropogenic emission inventory of atmospheric pollutants from sector- and fuel-specific sources (1970–2017): an application of the Community Emissions Data System (CEDS). *Earth System Science Data* **12**, 3413–3442 (2020). URL https://essd.copernicus.org/articles/12/3413/2020/.

[56] van Marle, M. J. E. *et al.* Historic global biomass burning emissions for CMIP6 (BB4CMIP) based on merging satellite observations with proxies and fire models (1750–2015). *Geoscientific Model Development* **10**, 3329–3357 (2017). URL https://gmd.copernicus.org/articles/10/3329/2017/.

[57] Kaiser, J. W. *et al.* Biomass burning emissions estimated with a global fire assimilation system based on observed fire radiative power. *Biogeosciences* **9**, 527–554 (2012). URL https://bg.copernicus.org/articles/9/527/2012/.

[58] Ghan, S. J. Technical Note: Estimating aerosol effects on cloud radiative forcing. *Atmospheric Chemistry and Physics* **13**, 9971–9974 (2013). URL https://acp.copernicus.org/articles/13/9971/2013/.

[59] Hasekamp, O., Litvinov, P., Fu, G., Chen, C. & Dubovik, O. Algorithm evaluation for polarimetric remote sensing of atmospheric aerosols. *Atmospheric Measurement Techniques* **17**, 1497–1525 (2024). URL https://amt.copernicus.org/articles/17/1497/2024/.

[60] Nakajima, T. & King, M. D. Determination of the Optical Thickness and Effective Particle Radius of Clouds from Reflected Solar Radiation Measurements. Part I: Theory. *Journal of the Atmospheric Sciences* **47**, 1878–1893 (1990). URL https://journals.ametsoc.org/view/journals/atsc/47/15/1520-0469_1990_047_1878_dotota_2_0_co_2.xml.

[61] Platnick, S. *et al.* The NASA MODIS-VIIRS Continuity Cloud Optical Properties Products. *Remote Sensing* **13**, 2 (2021). URL https://www.mdpi.com/2072-4292/13/1/2.

[62] Grosvenor, D. P. *et al.* Remote Sensing of Droplet Number Concentration in Warm Clouds: A Review of the Current State of Knowledge and Perspectives. *Reviews of Geophysics* **56**, 409–453 (2018). URL https://onlinelibrary.wiley.com/doi/abs/10.1029/2017RG000593.

[63] Donovan, D. P., van Zadelhoff, G.-J. & Wang, P. The EarthCARE lidar cloud and aerosol profile processor (A-PRO): the A-AER, A-EBD, A-TC, and A-ICE products. *Atmospheric Measurement Techniques* **17**, 5301–5340 (2024). URL https://amt.copernicus.org/articles/17/5301/2024/.

[64] Wandinger, U. *et al.* HETEAC – the Hybrid End-To-End Aerosol Classification model for EarthCARE. *Atmospheric Measurement Techniques* **16**, 2485–2510 (2023). URL https://amt.copernicus.org/articles/16/2485/2023/.

[65] van Zadelhoff, G.-J., Donovan, D. P. & Wang, P. Detection of aerosol and cloud features for the EarthCARE atmospheric lidar (ATLID): the ATLID FeatureMask (A-FM) product. *Atmospheric Measurement Techniques* **16**, 3631–3651 (2023). URL https://amt.copernicus.org/articles/16/3631/2023/.

[66] Schutgens, N. a. J., Partridge, D. G. & Stier, P. The importance of temporal collocation for the evaluation of aerosol models with observations. *Atmospheric Chemistry and Physics* **16**, 1065–1079 (2016). URL https://acp.copernicus.org/articles/16/1065/2016/.

[67] Watson-Parris, D., Williams, A., Deaconu, L. & Stier, P. Model calibration using ESEm v1.1.0 – an open, scalable Earth system emulator. *Geoscientific Model Development* **14**, 7659–7672 (2021). URL https://gmd.copernicus.org/articles/14/7659/2021/.

[68] Johnson, J. S. *et al.* The importance of comprehensive parameter sampling and multiple observations for robust constraint of aerosol radiative forcing. *Atmospheric Chemistry and Physics* **18**, 13031–13053 (2018). URL https://acp.copernicus.org/articles/18/13031/2018/.

[69] Williamson, D. *et al.* History matching for exploring and reducing climate model parameter space using observations and a large perturbed physics ensemble. *Climate Dynamics* **41**, 1703–1729 (2013). URL https://doi.org/10.1007/s00382-013-1896-4.

[70] Press, W., Teukolsky, S., Vetterling, W. & Flannery, B. *Numerical Recipes 3rd Edition: The Art of Scientific Computing* (Cambridge University Press, 2007).

Supplementary Files

This is a list of supplementary files associated with this preprint. Click to download.

- Supplementary.pdf